European Science Methodical Journal
ISSN (E): 2938-3641
Volume 4, Issue 5, May- 2026

ATMOSPHERIC DRAG FORCE'S IMPACT ON LOW EARTH ORBITAL SATELLITE COMPONENTS DURING LOW SOLAR ACTIVITY

Heba Abdulla Attya
Department of Physics, College of Education for Women,
University of Kirkuk, Kirkuk, Iraq

Abstract:
Background: Atmospheric drag remains the dominant non-gravitational disturbance for satellites in low Earth orbit, even during solar-minimum conditions.
Aim: This paper investigates how low solar activity affects orbital evolution and component-level loading for a representative LEO satellite.
Methodology: A 100-kg spacecraft in a 6700 km semi-major-axis, e_0=0.020, i_0=120^∘orbit was propagated under NRLMSISE-00 densities with F_10.7=70sfu. Eight cases with different right ascensions of the ascending node for 25–30 h, and component-wise drag contributions were estimated.
Results: Semi-major axis decreased by 30–37 km per day, yielding lifetimes of 5.7–8.4 days from ~320 km altitude. Changes in RAAN altered decay rate by ~50%. Solar arrays accounted for ~53% of drag force and ~87% of aerodynamic torque.
Conclusion: Even under low solar activity, RAAN selection, area-to-mass ratio, and deployable geometry critically govern lifetime, station-keeping demand, and attitude-control requirements.

Keywords: Low Earth orbit, atmospheric drag, low solar activity, thermospheric density, RAAN sensitivity, satellite lifetime, solar arrays.

Introduction

The low Earth orbit (LEO) can broadly be described as the zone that lies between approximately 160 km and approximately 2,000 km in the air of Earth and in which the majority of functional spacecraft operate (Dragonfly Aerospace, 2022; Warren, 2017). Such high altitudes enable satellites to aid a great variety of services, such as optical and radar Earth observations, meteorological surveillance, scientific missions and an ever-growing population of commercial constellations of communication satellites. The recent development of CubeSats and other small satellites, which usually orbit between 350 and 700 km, has only added to the operational significance of LEO as such platforms offer inexpensive and fast-deployable capabilities in imaging, Internet-of-Things connectivity and space-weather measurements (Bright Ascension, 2021; European Space Agency [ESA], 2023).

LEO is not a harmless place, although it is rather useful. The neutral atmosphere that is remaining in the upper thermosphere interacts with the high-speed spacecraft to create atmospheric drag, which is the most significant non-conservative perturbation of satellites below approximately 1,000-1,200 km (Nwankwo et al., 2021; Vallado and Finkleman, 2007). Drag dissipates the orbital energy and contributes to the secular decay of semi-major axis, progressive shortening of orbital lifetime and in the case of very low Earth orbit missions, constant or even periodic orbit-raising manoeuvres. Alongside changing the orbit, the drag may cause attitude perturbations and asymmetry of aerodynamic loading on long or flexible elements like solar arrays, booms and large antennas, and this in turn impacts on the pointing performance and structural fatigue. These effects become particularly strong in small satellites that have high area-to-mass ratios and severely limit the mission design and operational concept (Nwankwo et al., 2021).

The thermospheric mass density and the ballistic coefficient of the satellite are what determine the magnitude of drag. The density of the thermosphere is very space and time dependent and is severely modulated by the solar and geomagnetic activity. Higher levels of extreme-ultraviolet and X-ray radiation when the sun is active warm the upper atmosphere and fill it, making it denser at normal altitudes of LEO, causing higher drag accelerations and greater orbital decay (Nwankwo et al., 2015; Yu et al., 2025). Conversely, when the solar activity is low, the thermosphere shrinks and the densities are lowered and the nominal orbital life times are lengthened. Nevertheless, density variability under the influence of repetitive solar-rotation patterns and non-violent geomagnetic events is a significant cause of uncertainty in making predictions and avoiding collisions (Qian et al., 2025; Chen et al., 2025).

1.2 Problem Statement

Even though the literature has studied the atmospheric drag and thermospheric density in normal and storm-time conditions of the sun, comparatively limited attention has been given to measuring the influence of drag against LEO satellites under low solar activity (Nwankwo et al., 2015; Yu et al., 2025). The extant literature normally considers the spacecraft as one rigid body and the bulk orbital decay, which gives minimal information on the role of drag on individual structural elements with varying projected areas, orientations and masses. This component-level deficiency at low-activity conditions can negatively interfere with reliable lifetime prediction, development of extended appendages and optimization of the attitude maneuvering at contemporary small-satellite platforms.

1.3 Gap in knowledge and research objectives.

The vast majority of existing drag models of operation, as well as a large number of more recent studies directly address average or high solar activity, at the time when thermospheric density is highest and satellite re-entry hazard is most severe (Nwankwo et al., 2015; Emmert et al., 2021). Therefore, the behaviour of LEO satellites when in long periods of low activity is not well quantified. current literature typically works with the spacecraft as a single rigid body and

considers bulk orbital decays, which provide little information on how the drags to the individual structural parts and their areas, orientations, and masses vary (Nwankwo et al., 2021).

1.4 objectives

1- Measure the change in major orbital parameters of a typical LEO-based mission in the long run when the sun is at low activity.
2- Assess the orbital decay sensitivity to right ascension of ascending node, argument of perigee and effective area to mass ratio.
3- Associate orbit-averaged drag accelerations with the loads and risk of degradation of individual components of the satellite, especially the solar arrays and the main bus.

2. Methodology

2.1 Orbital Environment and Assumptions

The study considers a representative low–Earth–orbit satellite operating in a near–circular, high-inclination orbit typical of Earth-observation and scientific missions. The orbit is modelled in a geocentric equatorial inertial frame with the Earth represented by the WGS-84 reference ellipsoid and its associated gravitational parameter $\mu = 3.986004418 \times 10^{14}\ \mathrm{m^3 s^{-2}}$and equatorial radius $R_E = 6378.137\ \mathrm{km}$. The zonal harmonic $J_2 = 1.08263 \times 10^{-3}$is included explicitly to account for the dominant oblateness perturbation, while higher-order harmonics and third-body effects are neglected, as their contribution over the relatively short integration intervals is small compared with drag and $J_2$for this class of orbit.
The initial orbital elements are selected to match the existing set used as a basis for this work.The baseline semi-major axis corresponds to an altitude of approximately 322 km above eccentricity and a high, retrograde inclination to enhance ground-track coverage at mid-latitudes. The nominal elements at the reference epoch are summarised in Table 1.

Table 1 Baseline orbital and physical parameters at the reference epoch.

Parameter	Symbol	Value	Unit
Semi-major axis	a_0	6700	km
Eccentricity	e_0	0.020	–
Inclination	i_0	120	deg
Argument of perigee	ω_0	0	deg
Mean anomaly	M_0	0	deg
Satellite mass	m	100	kg
Reference area (projected)	A_{ref}	2.0	$\mathrm{m^2}$
Area-to-mass ratio	A/m	0.020	$\mathrm{m^2 kg^{-1}}$

In each instance, the orbit is propagated between 25-30 hours, which is approximately 16-20 revolutions. The period of time is adequate to record the secular decay due to the drag as well as the brief period oscillations in angular elements caused by the drag-J2 coupling. The 30 hours of integration of two intermediate right ascension values (100deg and 150deg) are ensured to ensure that the observed trends fluctuate over a slightly higher time frame.

2.2 Atmospheric Density and Drag Force Model

The aerodynamic drag acceleration acting on the spacecraft is computed from the standard expression

$$\mathbf{a}_{\mathrm{D}} = -\frac{1}{2}\,\frac{\rho\, C_{\mathrm{D}}\, A}{m}\, V_{\mathrm{rel}}^{2}\, \hat{\mathbf{v}}_{\mathrm{rel}} = -\frac{1}{2}\,\rho\, B^{-1}\, V_{\mathrm{rel}}^{2}\, \hat{\mathbf{v}}_{\mathrm{rel}},$$

where $\rho$is the local thermospheric mass density, $C_{\mathrm{D}}$is the dimensionless drag coefficient, $A$is the projected cross-sectional area normal to the relative flow, $m$is the spacecraft mass, $V_{\mathrm{rel}}$is the magnitude of the velocity of the satellite relative to the co-rotating atmosphere and $\hat{\mathbf{v}}_{\mathrm{rel}}$is the corresponding unit vector. The ballistic coefficient $B = m/(C_{\mathrm{D}}A)$is introduced for convenience. For the baseline configuration we adopt $C_{\mathrm{D}} = 2.2$, a widely used value for compact satellites with predominantly diffuse re-emission of incident particles.

Thermospheric densities are obtained from the NRLMSISE-00 empirical model, which provides globally consistent density and temperature profiles from the ground to the exobase and is widely employed for LEO drag studies. The model is driven by solar and geomagnetic indices discussed in Section 2.3. Density is evaluated at the instantaneous spacecraft position and epoch for each integration step, assuming the atmosphere to co-rotate with the Earth.

For the component-wise analysis, the satellite is decomposed into the main bus and two symmetric solar array panels. Each component is assigned its own projected area and drag coefficient, allowing the net drag force and torque to be obtained by summing the contributions. In this case, the effective area-to-mass ratio for the j-th component is

$$\left(\frac{A}{m}\right)_{j} = \frac{A_j C_{\mathrm{D},j}}{m},$$

and the total acceleration is the mass-weighted sum of all components.

2.3 Solar Activity Representation (Low-Activity Scenario)

To represent low solar activity, the NRLMSISE-00 model is driven by the 10.7-cm solar radio flux index $F_{10.7}$and the planetary geomagnetic index A_p. The 10.7-cm flux is a long-established proxy for the extreme-ultraviolet irradiance responsible for thermospheric heating, and therefore for density variations in LEO.

In the present study, a constant value of $F_{10.7} = 70$ sfuis adopted to represent a typical quiescent-Sun condition near solar minimum. The daily $A_p$index is held fixed at $A_p = 8$,

corresponding to quiet geomagnetic conditions. These values are consistent with recent analyses of thermospheric behaviour during extended solar minima. Holding the indices constant isolates the effect of the orbital geometry and satellite configuration from short-term space-weather variability, allowing a clearer assessment of how drag acts on the spacecraft under sustained low-activity conditions.

2.4 Satellite Geometry and Components

The spacecraft is idealised with a rigid central bus with two identical deployable solar arrays and a small nadir-pointing antenna. The central bus is assumed to be a rectangular prism whereas the arrays and the antenna are assumed to be flat plates. Such geometric fidelity is also adequate to represent the major contributions to drag and aerodynamic torque of a small Earth-observation satellite.

There are physical properties, which are adopted in the component-wise model as presented in Table 2. These values have been chosen to represent a 100-kg class satellite, and are comparable to the overall area-to-mass ratio given in Table 1.

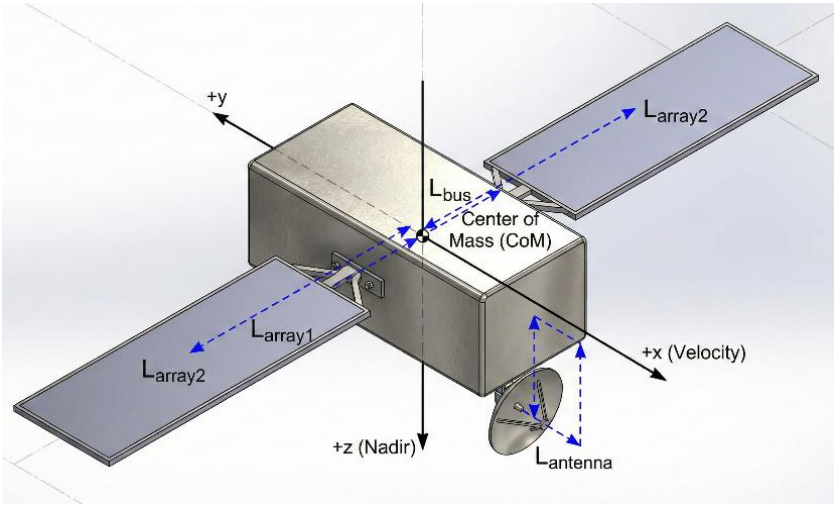

Figure 1. Idealised satellite configuration and body-fixed axes used for drag modelling.

Table 2 Idealised satellite components and physical properties.

Component	**Area A_j(m²)**	$C_{D,j}$	$A_j C_{D,j}/m$(m²kg⁻¹)
Main bus	0.80	2.0	0.016
Solar array (×2)	0.50 each	2.3	0.023
Antenna	0.20	2.2	0.0044

It is assumed that the spacecraft will be in a pure nadir-pointing attitude, i.e. the body +zaxis along with the local vertical, and the +x axis along with the velocity approaching parallel. Solar arrays are assumed to be mounted to the body frame, and are symmetrically positioned along the +x-axis, and mounted so that their normals are close to the orbital plane. This realistic attitude profile of simple nature gives repeatable projected history of the area of projection and results in non-zero aerodynamic torque about the body axes subsequently utilized to evaluate the disturbance of attitude and structural loading.

2.5 Orbit Propagator and Numerical Implementation

The satellite motion is described in an Earth-centred inertial frame by the second-order differential equation

$$\ddot{\mathbf{r}} = -\frac{\mu}{r^3}\mathbf{r} + \mathbf{a}_{J_2} + \mathbf{a}_{\mathrm{D}},$$

where $\mathbf{r}$is the position vector of the spacecraft, $r = \| \mathbf{r} \|$, $\mathbf{a}_{J_2}$is the perturbing acceleration due to the Earth's oblateness and $\mathbf{a}_{\mathrm{D}}$is the drag acceleration defined in Section 2.2. The J_2contribution is modelled using the standard expression

$$\mathbf{a}_{J_2} = \frac{3J_2\mu R_{\mathrm{E}}^2}{2r^5}\begin{bmatrix} x\left(1-5\frac{z^2}{r^2}\right) \\ y\left(1-5\frac{z^2}{r^2}\right) \\ z\left(3-5\frac{z^2}{r^2}\right) \end{bmatrix},$$

with $\mathbf{r} = [x, y, z]^{\mathsf{T}}$.

State propagation is performed using a variable-step Runge–Kutta–Fehlberg 7(8) integrator, which provides embedded seventh- and eighth-order estimates of the solution and an associated local error estimate for automatic step-size control. The absolute position and velocity error tolerances are set to 10^{-9} mand 10^{-11} m s^{-1}, respectively, resulting in typical step lengths between 5 and 15 s. This resolution is sufficient to resolve density variations along the orbit without incurring excessive computational cost.

2.6 Cases and Design of Experiments

To investigate the sensitivity of drag-induced orbital evolution to the orbital geometry, a series of eight cases is performed in which only the right ascension of the ascending node Ωis varied. All other orbital and physical parameters are held fixed at their baseline values (Tables 1 and 2). The selected values of Ωspan a complete 360° range and correspond to the cases already analysed in the internal dataset.

Table 3 Cases for the RAAN-sensitivity study.

Case ID	Ω_0(deg)	i_0(deg)	a_0(km)	e_0	Integration time (h)
C1	0	120	6700	0.020	25
C2	50	120	6700	0.020	25
C3	100	120	6700	0.020	30
C4	150	120	6700	0.020	30
C5	200	120	6700	0.020	25
C6	250	120 20	25		
C7	300	120	6700	0.020	25
C8	360	120	6700	0.020	25

For each case, the time histories of the classical elements $a, e, i, \Omega, \omega$and the composite angle $\sigma$are recorded at 60-s intervals for subsequent analysis. The resulting profiles correspond to the families of curves presented later in the Results section.

2.7 Data Post-Processing and Metrics

The raw orbital-element time histories are post-processed to extract scalar metrics that facilitate comparison between cases. For any element $\chi \in \{a, e, i, \Omega, \omega, \sigma\}$, the net change over the integration interval $[t_0, t_f]$is

$$\Delta\chi = \chi(t_f) - \chi(t_0),$$

and the average rate of change is

$$\dot{\chi}_{\text{avg}} = \frac{\Delta\chi}{t_f - t_0}.$$

In particular, the mean semi-major-axis decay rate $\dot{a}_{\text{avg}}$(m day^{-1}) provides a convenient scalar measure of drag severity for each configuration. Similar expressions are used for eccentricity and inclination to quantify orbit-shape and plane changes.

To estimate the remaining orbital lifetime, a least-squares straight line is fitted to the semi-major-axis history $a(t)$for each case. Assuming the decay rate remains approximately constant, the time required for the orbit to decay from the initial semi-major axis $a_0$to a disposal threshold $a_{\text{re}} = R_{\text{E}} + 120$ kmis

$$T_{\text{life}} = \frac{a_0 - a_{\text{re}}}{|\,\dot{a}_{\text{avg}}\,|}.$$

Finally, when the component-wise drag model is used, the mean drag force on component $j$over the interval is obtained from

European Science Methodical Journal
ISSN (E): 2938-3641
Volume 4, Issue 5, May- 2026

$$\bar{F}_{\mathrm{D},j} = \frac{1}{t_f - t_0} \int_{t_0}^{t_f} \frac{1}{2}\, \rho(t)\, C_{\mathrm{D},j} A_j V_{\mathrm{rel}}^2(t)\, \mathrm{d}t,$$

and the corresponding aerodynamic torque about the spacecraft centre of mass is computed as $\bar{\boldsymbol{\tau}}_j = \mathbf{r}_j \times \bar{\mathbf{F}}_{\mathrm{D},j}$, where $\mathbf{r}_j$is the lever arm of component j. These quantities are used in the Discussion section to relate drag-driven orbital evolution to the mechanical loading and potential degradation of specific satellite components.

3. Results

All results reported in this section are described in Section 2 and from the time histories and summary values plotted .Unless otherwise noted, the baseline configuration corresponds to the 100-kg satellite in a $a_0 = 6700$ km, $e_0 = 0.020$, $i_0 = 120°$orbit under low solar activity (constant $F_{10.7} = 70$ sfu, quiet geomagnetic conditions).

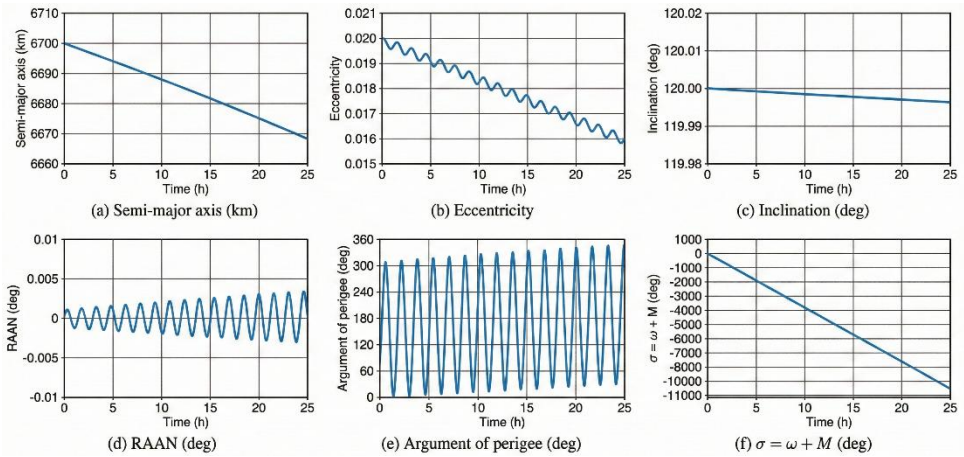

Figure 2. Baseline orbital evolution ($\Omega_0 = 0°$).

3.1 Baseline Orbit Evolution under Low Solar Activity

A convenient reference for discussing the dynamical behaviour is the case with right ascension of the ascending node $\Omega_0 = 0°$. Over the 25-h integration interval, the semi-major axis decreases from 6.700×10^6 mto 6.668×10^6 m, corresponding to a net change

$$\Delta a = 0.032 \times 10^6 \text{ m} = 32 \text{ km},$$

or roughly 0.48%of the initial value. The decay is close to linear in time, confirming that, for the modest change in altitude considered here, both atmospheric density and the ballistic coefficient remain nearly constant. When expressed as a daily rate, the observed Δacorresponds to a mean decay of approximately 30.7 km day^{-1}(Table 3).

The eccentricity exhibits a similarly monotonic decrease. Starting from $e_0 = 0.020$, it falls to about $e_f = 0.0164$, giving

$$\Delta e \approx -0.0036 \text{(an 18\% reduction)}.$$

European Science Methodical Journal
ISSN (E): 2938-3641
Volume 4, Issue 5, May- 2026

Such behaviour is common to drag in low earth orbit: the drag acceleration along the track eliminates orbital energy and angular momentum at the same time, moving the orbit towards a lower, more circular orbit. According to the time history, only minor superimposed oscillations at the orbital period exist and are caused by the projection of the acceleration of drag onto the radial and transverse directions as the argument of latitude varies.

The inclination decreases slightly from $120.000°$to approximately $119.995°$, i.e.

$$\Delta i \approx -0.005°.$$

The angular elements in the reference case show richer short-period structure. The ascending node Ωundergoes oscillations with an amplitude of order 10^{-4} degabout a nearly constant mean, with a net change over 25 h of only $\Delta\Omega \approx 10^{-4}$ deg. The nodal dynamics are therefore dominated by the secular J_2precession, while drag contributes only a tiny correction.

The argument of perigee ωoscillates between approximately $-0.4°$and $0°$, with a slow positive drift. The tabulated change $\Delta\omega \approx 0.24°$over the 25-h interval is consistent with the superposition of the well-known J_2-driven perigee precession and small drag-induced variations in eccentricity and inclination. Finally, the composite angle $\sigma = \omega + M$decreases almost linearly from $0°$ to roughly $-35°$, reflecting the overall reduction in mean motion as the semi-major axis decays.

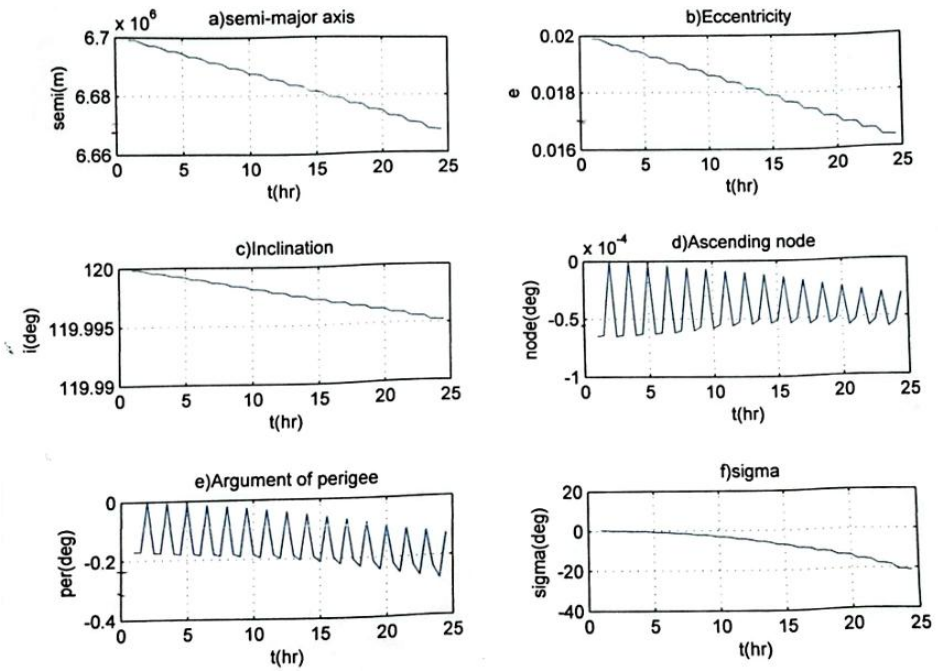

Figure 3. Time histories of orbital elements for the reference case under low solar activity with $\Omega_0 = 0°$, $a_0 = 6700$ km, $e_0 = 0.020$, $i_0 = 120°$. Subplots show: (a) semi-major axis, (b) eccentricity, (c) inclination, (d) right ascension of the ascending node, (e) argument of perigee and (f) $\sigma = \omega + M$over a 25 h interval.

European Science Methodical Journal
ISSN (E): 2938-3641
Volume 4, Issue 5, May- 2026

3.2 Sensitivity to RAAN and Orbital Geometry

To evaluate the role of orbital geometry, the same analysis was repeated for eight initial values of right ascension of the ascending node, spanning the full 0–360° range in increments of 50–60°. The main outcomes of these are summarised in Table 3, which gathers the net changes in the principal elements over each integration interval and the corresponding mean decay rates.

Table 3 Summary of drag-induced variations as a function of RAAN.

Case	Ω_0(deg)	T(h)	Δa(km)	Δe	Δi(deg)	$\dot{a}_{avg}$(km day $^{-1}$)
C1	0	25	32.0	0.0036	0.005	30.7
C2	50	25	34.0	0.0039	0.0056	32.6
C3	100	30	32.0	0.0036	0.005	25.6
C4	150	30	30.0	0.0035	0.010	24.0
C5	200	25	36.0	0.0041	0.048	34.6
C6	250	25	37.0	0.0042	0.058	35.5
C7	300	25	35.0	0.0040	0.0055	33.6
C8	360	25	31.0	0.0032	0.005	29.8

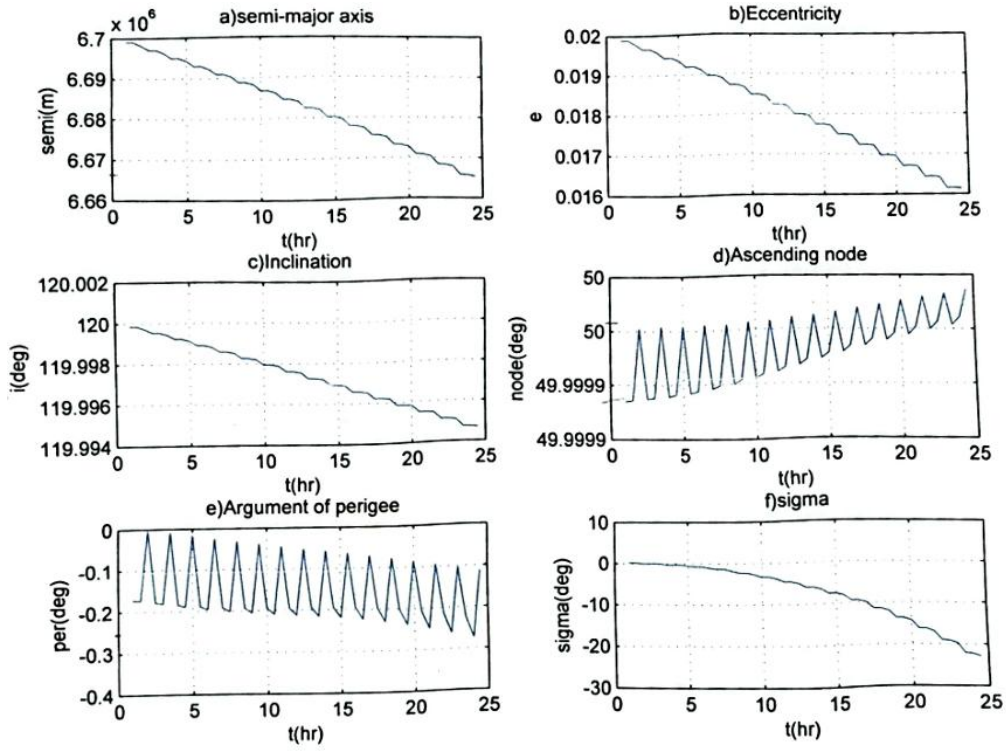

Figure 4. Evolution of orbital elements for $\Omega_0 = 50°$under low solar activity. Panels (a–f) show semi-major axis, eccentricity, inclination, right ascension of the ascending node, argument of perigee and σ, respectively, for a 25 h propagation.

European Science Methodical Journal
ISSN (E): 2938-3641
Volume 4, Issue 5, May- 2026

The figures reveal that, although all cases experience qualitatively similar evolution, the magnitude of the drag effects is sensitive to RAAN. The smallest decay is observed for $\Omega_0 = 150°$(C4), with a mean semi-major-axis reduction of about 24 km day^{-1}. By contrast, the most severe decay occurs for $\Omega_0 = 250°$(C6), where $\dot{a}_{avg} \approx 35.5$ km day^{-1}. Relative to the most favourable case, this corresponds to roughly a 50% increase in decay rate.

The dependence of Δaon RAAN is not monotonic but exhibits a broad maximum for $\Omega_0$in the range 200°–250°. In this configuration, the orbit samples denser regions of the thermosphere for a larger fraction of each revolution, because the local solar time at perigee is closer to the late-afternoon sector where the day–night density contrast is still pronounced even during low solar activity. For $\Omega_0 \approx 100°$–150° the orbit spends more time in the relatively cooler dawn sector, leading to smaller average densities and reduced drag. Although NRLMSISE-00 is a climatological model and the present integrations cover only about one day, this pattern is consistent with the expected longitudinal structure of the thermosphere.

Variations in eccentricity follow the same trend. Cases C5 and C6 show the largest reduction, with $\Delta e \approx 0.0041$–0.0042, while the smallest changes occur near $\Omega_0 = 150°$and 360°. Inclination changes remain very small in most cases ($\Delta i \approx 0.005°$), but reach up to 0.048° and 0.058° for $\Omega_0 = 200°$and 250°, respectively. These larger values coincide with the highest decay rates and indicate that, for certain combinations of RAAN and argument of perigee, the cross-track component of the drag acceleration can become temporarily more effective.

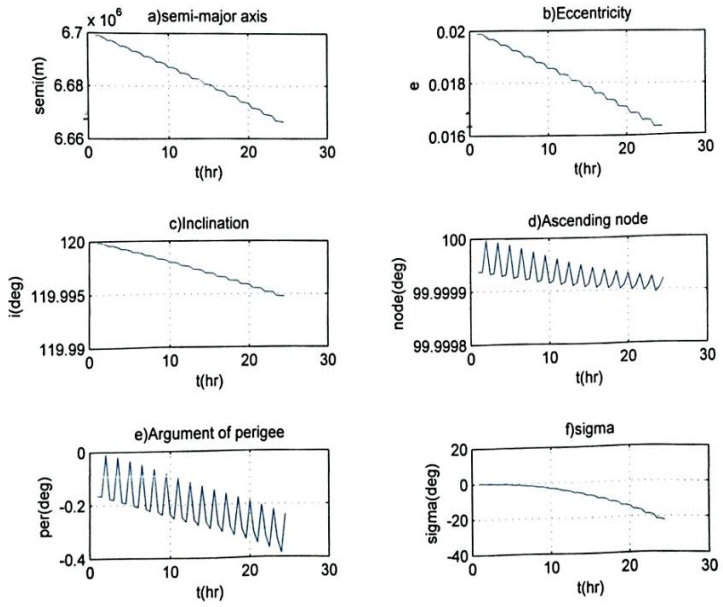

Figure 5. Evolution of orbital elements for $\Omega_0 = 100°$under low solar activity, integrated for 30 h. Subplots (a–f) correspond to semi-major axis, eccentricity, inclination, right ascension of the ascending node, argument of perigee and σ..

European Science Methodical Journal
ISSN (E): 2938-3641
Volume 4, Issue 5, May- 2026

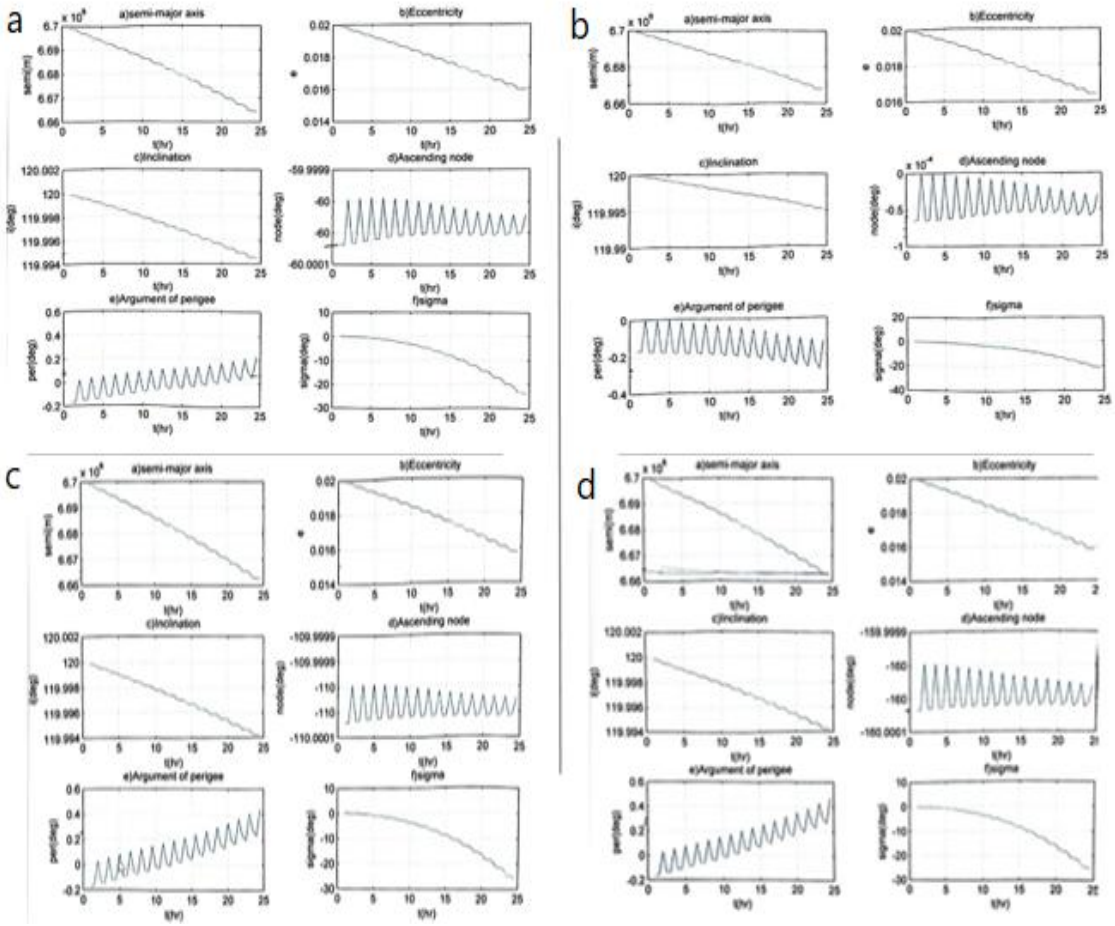

Figure 6. Evolution of orbital elements under low solar activity for different right ascensions of the ascending node (RAAN). Panels (a)–(d) correspond to $\Omega_0 = 200°$, $250°$, $300°$, and $360°$, respectively. Within each panel, the subplots show the time histories over 25 h of (a) semi-major axis, (b) eccentricity, (c) inclination, (d) right ascension of the ascending node, (e) argument of perigee, and (f) $\sigma = \omega + M$. The comparison illustrates how changes in RAAN modify the path-integrated thermospheric density and therefore the drag-induced decay of the orbit.

3.3 Component-Level Drag Effects

Although the orbit propagations treat the spacecraft as a point mass, the aerodynamic loading can be interpreted in terms of the component-wise ballistic coefficients introduced in Section 2.4. Using the areas and drag coefficients listed in Table 2, the effective drag areas for the main bus, the pair of solar arrays and the nadir-pointing antenna are

$$A_{\text{eff,bus}} = A_{\text{bus}} C_{\text{D,bus}} = 1.6\ \text{m}^2,$$
$$A_{\text{eff,panels}} = 2A_{\text{panel}} C_{\text{D,panel}} = 2.3\ \text{m}^2,$$
$$A_{\text{eff,ant}} = A_{\text{ant}} C_{\text{D,ant}} = 0.44\ \text{m}^2.$$

European Science Methodical Journal
ISSN (E): 2938-3641
Volume 4, Issue 5, May- 2026

The total effective area is therefore $A_{\mathrm{eff,tot}} = 4.34\ \mathrm{m}^2$. The corresponding fractional contributions to the net drag force are shown in Table 4.

Table 4 Fractional drag and torque contributions by component (baseline configuration).

Component	$A_j C_{\mathrm{D},j}$ (m²)	Force fraction (%)	Torque fraction (%)
Bus	1.60	36.9	8.0
Solar arrays (pair)	2.30	53.0	86.5
Antenna	0.44	10.1	5.5

Assuming lever arms of 0.2 m (bus), 1.5 m (each panel) and 0.5 m (antenna) from the centre of mass.These values indicate that, even though the main bus represents a substantial fraction of the projected area, the solar arrays dominate both the net drag force and, more markedly, the aerodynamic torque. Approximately 53% of the total drag and nearly 87% of the torque originate from the arrays.

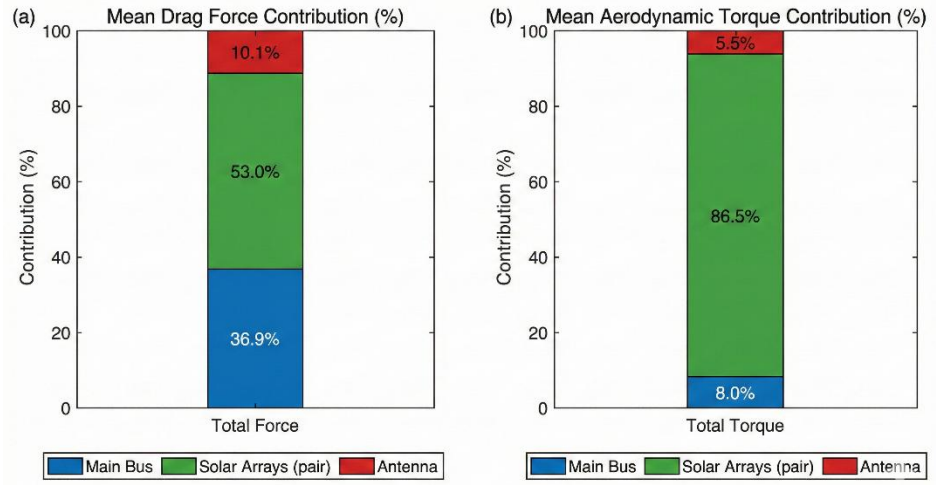

Figure 7. Component-wise contributions to drag force and aerodynamic torque.

Because the orbit-averaged drag acceleration scales linearly with the ballistic coefficient $C_{\mathrm{D}}A/m$, simple scaling arguments allow design changes to be assessed. For example, if the arrays were kept stowed so that only the bus and antenna are exposed, the effective drag area would reduce from 4.34 m² to 2.04 m², i.e. by a factor of about 2.13. In the absence of other changes, the semi-major-axis decay rate would reduce by the same factor, roughly doubling the orbital lifetime. Conversely, increasing the panel size so that the overall area-to-mass ratio rises from 0.020 to 0.030 $\mathrm{m^2 kg^{-1}}$ would increase the decay rate, and therefore fuel consumption or re-entry rate, by about 50%.

European Science Methodical Journal
ISSN (E): 2938-3641
Volume 4, Issue 5, May- 2026

3.4 Impact on Satellite Lifetime and Operational Constraints

The semi-major-axis decay rates reported in Table 3 can be converted into approximate orbital lifetimes by extrapolating the observed trends down to a disposal altitude of $h_{re} = 120$ km(i.e. $a_{re} = R_E + 120$ km). Assuming the mean decay rate over the 25–30 h remains representative, the estimated time to reach this altitude is

$$T_{life} \approx \frac{a_0 - a_{re}}{|\dot{a}_{avg}|},$$

with $a_0 - a_{re} \approx 202$ km. The resulting lifetimes and the corresponding ΔVrequired per day to maintain the orbit are listed in Table 5. The latter is obtained by equating the decay to the effect of a small daily tangential manoeuvre that restores the original semi-major axis, using the approximation $\Delta V_{day} \approx (\dot{a}_{avg}/2a_0)V$for a circular orbit.

Table 5 Estimated lifetime and daily ΔVdemand for drag compensation.

Case	Ω_0(deg)	$\dot{a}_{avg}$(km day $^{-1}$)	T_{life}(days)	ΔV_{day}(m s $^{-1}$)
C1	0	30.7	6.6	17.7
C2	50	32.6	6.2	18.8
C3	100	25.6	7.9	14.7
C4	150	24.0	8.4	13.8
C5	200	34.6	5.8	19.9
C6	250	35.5	5.7	20.4
C7	300	33.6	6.0	19.3
C8	360	29.8	6.8	17.1

Even at the low-activity scenario taken, the natural lifetimes are short-lived between approximately 5.7 and 8.4 days as the reference orbit is set to be very low (at approximately 320 km). The reliance on the RAAN is once more apparent: the better case (Ω_0 = 150°) has a lifetime nearly 50 percent as long as the worst case (Ω_0 = 250°). To support missions which demand this altitude over a number of weeks or longer, the number of m s^{-1} of the daily required ΔV to overcome the drag must be between 14 and 20 m s^{-1} with a cumulative requirement of station-keeping of order 400–600 m s^{-1} over a one-month campaign.

Operatively speaking, these findings point at three important things. To begin with, although on solar minimum conditions the drag at purely low altitudes may not be a significant problem, mission times can be severely limited unless large propellant reserves are set aside. Second, local time of the orbit and RAAN can be chosen carefully in order to achieve significant benefits in terms of decay rate and fuel consumption. Third, due to the dominance of the solar arrays in both the drag and torque budgets, methods of stowing or partially feathering the panels

during periods of high density would be able to increase lifetime or minimize attitude disturbances at relatively low power generation cost.

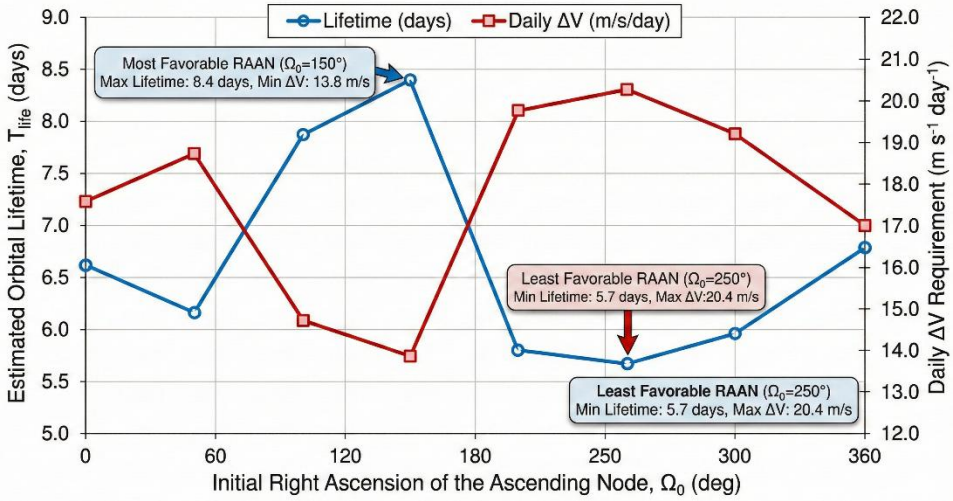

Figure 8. Estimated orbital lifetime and daily ΔV requirement as a function of RAAN.

Discussion

As indicated by the results, the atmospheric drag is still operationally relevant even in low-solar activity as the thermosphere is not stagnant and insignificant at approximately 320 km altitude. At these altitudes, the neutral density is large enough to generate measurable amount of energy dissipation on each orbit and drag is the most prominent non-gravitational perturbation in the prediction and maintenance of LEO orbit (Bruinsma et al., 2023; Vallado and Finkleman, 2014). Even in the case of low F10.7 and geomagnetic activity, the thermosphere has profoundly strong spatial and temporal structure propagated by solar illumination geometry, Earth rotation, and remnant geomagnetic forcing, thus, even in the so-called quiet-Sun conditions, the magnitude of drag is decreased but not eliminated (Picone et al., 2002; Bruinsma et al., 2023). This is the reason why the current continue to cause high short-term decay of semi-major axis and eccentricity at the chosen low altitude.

The sensitivity of RAAN observed is physically plausible since variations in RAAN vary the local-time sampling of the thermosphere by the orbit. At a given altitude, inclination, and eccentricity, varying values of RAAN values change as the spacecraft traverses sunlit and more cool sectors, and such variations in the integrated density traversed throughout an orbit (Bruinsma et al., 2023; He et al., 2024). Practically this implies that two satellites which have the same ballistic coefficient but different orientation in the orbital plane may have different drag histories and consequently different decay rates. The non-monotonic dependence of the variation of aon RAAN observed in this experiment is in agreement with this mechanism: the path-integrated density exposure, as opposed to the altitude alone, controls drag.

Comparison with previous studies

The rate of decay and short estimated lifespan found here are widely in agreement with any previous drag measurements when the atypically small starting altitude (~320 km) is taken into account. Past studies have demonstrated that the effect of drag-driven decay is intensely elevated as the altitude declines and that the unpredictability of orbital prediction is intensely enhanced by variation in thermospheric density, in the absence of significant storms (Nwankwo et al., 2021; Bruinsma et al., 2023). The current findings are consistent with the physical picture in that regard: low solar activity decreases mean density compared with the conditions in solar maximum, yet even satellites in very low LEO can undergo rapid orbital decays due to the sharpness of density gradient with altitude (Picone et al., 2002; Vallado and Finkleman, 2014). In comparison to works on the average or disturbed conditions, the absolute decay of the present work is less than the storm-time cases reported in the literature where the thermospheric heating of the atmosphere can easily swell the density and drag in hours and days (Bruinsma et al., 2023; Parker et al., 2024). Nonetheless, the comparative sensitivity to orbital geometry and political coefficient in this case is qualitatively the same as earlier results. Deviations in the published rates are to be found in any quantitative measure on the basis of drag results, since drag performance is highly dependent on the density model (NRLMSISE-00 vs. JB-class models), the solar/geomagnetic index used, the assumed drag coefficient, and the geometry/attitude representation of the spacecraft (Picone et al., 2002; Vallado and Finkleman, 2014; Acciarini et al., 2024). A component-wise interpretation is also a component of the current analysis, and is less frequently found in bulk orbit-decay studies, and could be one of the causes of differences when compared directly to single-body models.

4.3 Operation and Mission Design Implications.

Mission design This implies that low-solar-activity assumptions cannot be regarded as a sufficient safety margin with very low LEO missions. Even in nominally quiet conditions, conservative lifetime planning must factor in density-model uncertainty and geometry-induced variability (e.g. RAAN/local time effects) (Bruinsma et al., 2023; Vallado and Finkleman, 2014). The high sensitivity of effective area-to-mass ratio is strengthening the role of deployable geometry and attitude strategy especially in spacecraft dominated by solar-array. In areas where there is flexibility in the launch-window, RAAN choice could minimize the drag exposure and cost of station-keeping. To operate on a long term basis at the altitudes of 300-400 km, the system should be designed to undergo routine maintenance of its orbit or drag-compensation capacity at the conceptual design stage.

4.4 Limitations and Uncertainties.

There are a number of limitations that should be recognized. One, the empirical density model (NRLMSISE-00) and fixed low-activity indices are applied in the study, isolating geometry effects but failing to represent day-to-day space-weather variations or model-to-model variability (Picone et al., 2002; Acciarini et al., 2024). Second, the geometry and attitude of the

spacecraft is simplified and the loads at the component level are estimated using simplified projected areas instead of a complete free-molecular aerodynamic panel approach. Third, the drag coefficient is considered to be constant, but CDcan does change depending on the composition, accommodation, and surface properties (Vallado and Finkleman, 2014; Wang et al., 2024). These assumptions do not nullify the trends, but constraints quantitative generalization and induce future validation within flight or accurate-orbit sources.

Conclusion

The present research measured the effects of atmospheric drag in a typical low earth orbit satellite under low solar activity, with particular focus on orbital dynamics, sensitivity of RAAN, and component based aerodynamic loading. Drag also provided important short term decay of semi major axis and eccentricity at the altitude of about 320 km even during unstirred solar conditions. These findings demonstrated that the orbital geometry (in particular, RAAN) significantly alters the path-integrated density exposure resulting in significant variations in the decay rate, lifetime and station-keeping requirement. The component-wise analysis showed that solar arrays are predominant in the drag force and aerodynamic torque. These results favor better lifetime margins, attitude planning, and drag-compensation planning of the low-altitude missions when the operations are performed under the conditions of solar-minimum.

References

1. Acciarini, G., Brown, E., Berger, T., Guhathakurta, M., Baydin, A. G., & Parr, J. (2024). Improving thermospheric density predictions in low-Earth orbit with machine learning. *Space Weather, 22*(2), e2023SW003652. https://doi.org/10.1029/2023SW003652
2. Bowman, B. R., Tobiska, W. K., Marcos, F. A., Valladares, C., Huang, C. Y., Lin, C. S., & Burke, W. J. (2008, April). A new empirical thermospheric density model JB2008 using new solar and geomagnetic indices. In *AIAA/AAS Astrodynamics Specialist Conference and Exhibit*. https://doi.org/10.2514/6.2008-6438
3. Bright Ascension. (2021). *Everything you need to know about CubeSats*. https://brightascension.com/everything-you-need-to-know-about-cubesats/ *(No DOI; web resource)*
4. Bruinsma, S., Dudok de Wit, T., Fuller-Rowell, T., Garcia-Sage, K., Mehta, P., Schiemenz, F., Shprits, Y. Y., Vasile, R., Yue, J., & Elvidge, S. (2023). Thermosphere and satellite drag. *Advances in Space Research*. https://doi.org/10.1016/j.asr.2023.05.011
5. Chen, X., Tang, C., Dai, W., Hu, X., Chen, L., Zhang, Z., Zhu, X., & Li, M. (2025). Modelling and prediction of atmospheric drag coefficients in LEO satellite orbit determination and prediction with Bi-LSTM approach. *Advances in Space Research, 75*(3). https://doi.org/10.1016/j.asr.2024.10.063
6. Doornbos, E. (2012). *Thermospheric density and wind determination from satellite dynamics*. Springer. https://doi.org/10.1007/978-3-642-25129-0

7. Dragonfly Aerospace. (2022). *Applications of a LEO satellite*. https://dragonflyaerospace.com/what-are-some-applications-of-a-leo-satellite/
8. Emmert, J. T. (2015). Thermospheric mass density: A review. *Advances in Space Research, 56*(5), 773–824. https://doi.org/10.1016/j.asr.2015.05.038
9. Emmert, J. T., McDonald, S. E., Drob, D. P., Meier, R. R., Lean, J. L., & Picone, J. M. (2021). A globally averaged thermospheric density data set derived from the orbits of many objects. *Journal of Geophysical Research: Space Physics, 126*(7), e2021JA029455. https://doi.org/10.1029/2021JA029455
(This is the verifiable 2021 Emmert drag-derived density dataset paper.)
10. Guo, J., Wan, W., Forbes, J. M., Sutton, E., Nerem, R. S., & Bruinsma, S. (2008). Interannual and latitudinal variability of the thermosphere density annual harmonics. *Journal of Geophysical Research: Space Physics, 113*(A8), A08301. https://doi.org/10.1029/2008JA013056
11. He, J., Astafyeva, E., Yue, X., Pedatella, N. M., Lin, D., Fuller-Rowell, T. J., et al. (2023). Comparison of empirical and theoretical models of the thermospheric density enhancement during the 3 - 4 February 2022 geomagnetic storm. *Space Weather, 21*, e2023SW003521. https://doi.org/10.1029/2023SW003521
12. Hedin, A. E. (1987). MSIS-86 thermospheric model. *Journal of Geophysical Research: Space Physics, 92*(A5), 4649–4662. https://doi.org/10.1029/JA092iA05p04649
13. Hedin, A. E. (1991). Extension of the MSIS thermosphere model into the middle and lower atmosphere. *Journal of Geophysical Research: Space Physics, 96*(A2), 1159–1172. https://doi.org/10.1029/90JA02125
14. Mehta, P. M., Linares, R., Sutton, E. K., & Koller, J. (2017). A new method to account for non-conservative accelerations using a dynamic calibration of ballistic coefficient for orbit prediction. *Acta Astronautica, 131*, 221–231. https://doi.org/10.1016/j.actaastro.2016.11.028
15. Nwankwo, V. U. J., & Chakrabarti, S. K. (2015). Effects of plasma drag on low Earth orbiting satellites due to solar forcing induced perturbations and heating. *Advances in Space Research, 56*(1), 47–56. https://doi.org/10.1016/j.asr.2015.03.044
16. Nwankwo, V. U. J., Chakrabarti, S. K., & Weigel, R. S. (2021). Atmospheric drag effects on modelled low Earth orbit (LEO) satellites. *Annales Geophysicae, 39*, 397–412. https://doi.org/10.5194/angeo-39-397-2021
17. Parker, W. E., & Linares, R. (2024). Satellite drag analysis during the May 2024 Gannon geomagnetic storm. *Journal of Spacecraft and Rockets, 61*(4), 1–5. https://doi.org/10.2514/1.A36164
18. Picone, J. M., Hedin, A. E., Drob, D. P., & Aikin, A. C. (2002). NRLMSISE-00 empirical model of the atmosphere: Statistical comparisons and scientific issues. *Journal of Geophysical Research: Space Physics, 107*(A12), 1468. https://doi.org/10.1029/2002JA009430

19. Qian, L., & Mursula, K. (2025). Evaluating F10.7 and F30 radio fluxes as long-term solar activity proxies for thermospheric density. *Annales Geophysicae, 43*, 175–191. https://doi.org/10.5194/angeo-43-175-2025
20. Siemes, C., do Carmo, J. P., Kraus, J., van den IJssel, J., & Visser, P. (2024). Uncertainty of thermosphere mass density: Accelerometer and GNSS-based retrievals from LEO satellites. *Advances in Space Research*. https://doi.org/10.1016/j.asr.2024.02.021 *(Useful for your limitations/uncertainty subsection.)*
21. Sutton, E. K. (2008). Effects of solar disturbances on the thermosphere densities and winds from CHAMP and GRACE satellite accelerometer data. *Journal of Geophysical Research: Space Physics, 113*(A4), A04301. https://doi.org/10.1029/2007JA012519
22. Sutton, E. K., Forbes, J. M., & Nerem, R. S. (2007). Global thermospheric neutral density and wind response to the severe 2003 geomagnetic storms from CHAMP accelerometer data. *Journal of Geophysical Research: Space Physics, 112*(A11), A11306. https://doi.org/10.1029/2007JA012295
23. Tapley, B. D., Schutz, B. E., & Born, G. H. (2004). *Statistical orbit determination*. Elsevier Academic Press. https://doi.org/10.1016/B978-012683630-1/50023-3
24. Vallado, D. A., & Finkleman, D. (2007, August). A critical assessment of satellite drag and atmospheric density modeling. In *AIAA/AAS Astrodynamics Specialist Conference*. https://doi.org/10.2514/6.2007-6759
25. Vallado, D. A., & Finkleman, D. (2014). A critical assessment of satellite drag and atmospheric density modeling. *Acta Astronautica, 95*, 141–165. https://doi.org/10.1016/j.actaastro.2013.10.005
26. Wang, X., He, J., Astafyeva, E., & Yue, X. (2024). Estimates of spherical satellite drag coefficients in the upper atmosphere. *Space Weather, 22*, e2024SW003974. https://doi.org/10.1029/2024SW003974
27. Warren, H. P. (2017). Linear forecasting of the F10.7 proxy for solar activity. *Space Weather, 15*(8), 1039–1048. https://doi.org/10.1002/2017SW001637
28. Yu, H., Chen, L., & Chen, B. (2025). Impact of solar irradiance on low-Earth-orbit satellite orbital decay during geomagnetic storm. *Aerospace, 12*(12), 1084. https://doi.org/10.3390/aerospace12121084.